THE JOURNAL OF PHYSICAL CHEMISTRY Letters

pubs.acs.org/JPCL Letter

Fate of Low-Lying Charge-Transfer Excited States in a Donor:Acceptor Blend with a Large Energy Offset

Giacomo Londi, Saeed-Uz-Zaman Khan, Luca Muccioli, Gabriele D'Avino, Barry P. Rand, and David Beljonne*

Cite This: J. Phys. Chem. Lett. 2020, 11, 10219–10226 Read Online

ACCESS | Metrics & More | Article Recommendations | Supporting Information

ABSTRACT: In an effort to gain a comprehensive picture of the interfacial states in bulk heterojunction solar cells, we provide a combined experimental–theoretical analysis of the energetics and dynamics of low-lying electronic charge-transfer (CT) states in donor:acceptor blends with a large frontier orbital energy offset. By varying the blend composition and temperature, we unravel the static and dynamic contributions to the disordered density of states (DOS) of the CT-state manifold and assess their recombination to the ground state. Namely, we find that static disorder (conformational and electrostatic) shapes the CT DOS and that fast nonradiative recombination crops the low-energy tail of the distribution probed by external quantum efficiency (EQE) measurements (thereby largely contributing to voltage losses). Our results then question the standard practice of extracting microscopic parameters such as exciton energy and energetic disorder from EQE.

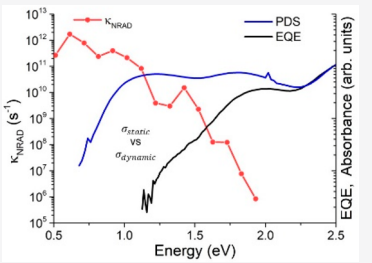

Organic solar cells (OSCs) have reached power conversion efficiencies (PCEs) close to 18%, with recent increases owing to the development of non-fullerene acceptors[1,2] and the engineering of donor:acceptor (D:A) bulk heterojunction (BHJ) interfaces. The current target is minimizing sources of energy losses, which in OSCs deal with the fate of tightly bound, intermolecular electron–hole (eh) pairs generated at the D:A interface upon charge transfer (CT).[3] The production of separated charges from those states requires that holes and electrons overcome their Coulomb binding energy instead of recombining to the ground state. These CT states come with their own density of states (DOS), which is typically quite broad for various reasons: D:A blends that often comprise a heterogeneous distribution of local microstructures; the coupling between the electronic excitations and the nuclear degrees of freedom; and the involvement of multiple electron and/or hole states. Despite several investigations, the detailed origin for the DOS and the role of hot versus relaxed CT states in charge separation and recombination are still controversial.[4−6]

One way to analyze the manifold of excited states is by means of external quantum efficiency (EQE) measurements, which provide a measure of the CT DOS, weighted by the contribution of the different states to the photocurrent.[7] Using this technique, we previously conducted a study on D:A systems characterized by wide optical bandgaps and a large driving force for charge separation, resulting in ultrabroad CT-state spectra.[8] Typically, such combinations of materials are also characterized by a small energy offset between the donor highest occupied molecular orbital (HOMO) and the acceptor lowest unoccupied molecular orbital (LUMO), leading to a low open-circuit voltage (V_{oc}). Although not at all appealing for their OSC performances, these systems are nevertheless an interesting case study for resolving the existing dilemmas about the nature and fate of interfacial CT states.

Here, we focus on NPB:HAT-CN blends at different compositions and temperatures. In an earlier report, we discussed the existence of multiple electronic CT states at these heterointerfaces and their contributions to the photocurrent.[8] In this work, we provide a comprehensive microscopic model for the energetics and dynamics of the first electronic CT state, disentangling the contributions from static and dynamic disorder to the DOS. Our computational protocol entails a combination of molecular dynamics (MD) simulations, density functional theory (DFT), and time-dependent (TD) DFT calculations, and a microelectrostatic (ME) model,[9,10] specifically designed to include environmental effects, as the electron affinity (EA) and ionization potential (IP) of molecules in a solid-state environment and the corresponding CT excitation energies depend on mutual intermolecular electrostatic interactions.[11] We observe that the CT DOS is broadened mostly because of conformational and electrostatic disorder associated with the NPB flexibility and the HAT-CN quadrupolar layout, respectively, and is essentially static on the time scale of charge separation/recombination. We also predict fast nonradiative decay from

Received: September 18, 2020
Accepted: November 13, 2020

https://dx.doi.org/10.1021/acs.jpclett.0c02858
J. Phys. Chem. Lett. 2020, 11, 10219–10226

the lowest CT states that should overcome charge separation, hence rendering these states EQE silent. This is fully confirmed by experimental absorption and EQE measurements showing that the CT DOS explored by EQE is cropped at low energy.

THEORETICAL METHODS

Three films of NPB and HAT-CN at different relative concentrations were prepared by vapor co-deposition on graphene, by means of *NVT* non-equilibrium MD simulations,[12−14] for a final film thickness exceeding in all cases 10 nm. The three systems were subsequently cooled and equilibrated at 300 K, and subsequently at 200 and 100 K. Molecular geometries were then extracted from the equilibrated configurations and used for electronic structure calculations. All simulations were performed with the NAMD code.[15]

Ionization potentials IP^{gas}_{NPB} and electron affinities $EA^{gas}_{HAT\text{-}CN}$ were computed at the gas-phase DFT level with the range-separated hybrid (RSH) functional ωB97X-D[16] along with the 6-311++G(d,p) basis set using the GAUSSIAN16 suite.[17] These transport levels were evaluated as total energy differences between charged and neutral species, applying a correction based on gas-phase GW calculations for the inaccuracies of the force field in describing molecular geometries.

The solid-state energy levels for holes on NPB and electrons on HAT-CN can be expressed as $IP_{NPB} = IP^{gas}_{NPB} + \Delta^{+}$ and $EA_{HAT\text{-}CN} = EA^{gas}_{HAT\text{-}CN} + \Delta^{-}$, where polarization energies for holes (Δ^{+}) and electrons (Δ^{-}) were obtained via ME calculations.[9,10] The energy of CT states was calculated for molecular NPB:HAT-CN pairs in close contact selected from MD samples. The photovoltaic gap is defined as $E_{GAP} = IP_{NPB} - EA_{HAT\text{-}CN}$. The optical gap is $E_{CT} = E_{GAP} + E_B$, where $E_B < 0$ is the Coulomb exciton interaction between closely spaced electron and holes. The latter is calculated with self-consistent ME calculations as the screened interaction between hole and electron charge densities.

The conformational disorder was assessed with gas-phase DFT calculations performed at the MD geometries, quantifying the fluctuations of the NPB HOMO and the HAT-CN LUMO. The high- and low-frequency contributions to the dynamic conformational disorder were separated by means of a Fourier filter procedure applied to the time series of molecular orbital energies computed along the MD trajectories at 300 K (see Table 1 and Figure S3). The variances of the frequency-filtered time series were averaged over five NPB and five HAT-CN molecules.

Nonradiative recombination rates κ_{NRAD} between the (first) CT state and the ground state were calculated with the semiclassical Marcus−Levich−Jortner (MLJ) expression:

$$\kappa_{NRAD} = \frac{2\pi}{\hbar} J^2 \sqrt{\frac{1}{4\pi\lambda_{env} k_B T}} \times \sum_n \left\{ \exp(-S_{eff}) \frac{S_{eff}^{\,n}}{n!} \times \exp\left[-\frac{(-E_{CT}^{0,0} + \lambda_{env} + n\hbar\omega_{eff})^2}{4\lambda_{env} k_B T} \right] \right\} \quad (1)$$

where J is the electronic coupling between those states, $\hbar$ is the reduced Planck's constant, k_B is the Boltzmann constant, T is the temperature in kelvin, λ_{env} is the environmental reorganization energy computed from σ_{low} as $\lambda_{env} = \frac{\sigma_{low}^{2x}}{2k_B T}$, $\omega_{eff} = 0.15$ eV is the energy of an effective high-frequency intramolecular vibration, $S = \lambda_{int}/(\hbar\omega_{eff})$ is the corresponding Huang−Rhys factor, and $E_{CT}^{0,0} = E_{CT} - \lambda_{int}$ is the GW/ME energy, where λ_{int} is removed to avoid double counting with the term $n\hbar\omega_{eff}$. The full treatment of the theoretical methodology is reported in the Supporting Information.

Table 1. Standard Deviations (in millielectronvolts) of the Intramolecular Energy Level Dynamic Fluctuations along the MD Trajectory, Partitioned into the Low (σ^{x}_{low})- and High-Frequency (σ^{x}_{high}) Component Disorder, with $\sigma^{x}_{dyn} = \sqrt{\sigma^{2x}_{low} + \sigma^{2x}_{high}}$ [a]

	NPB			HAT-CN		
%/T (K)	σ^{IP}_{low}	σ^{IP}_{high}	σ^{IP}_{dyn}	σ^{EA}_{low}	σ^{EA}_{high}	σ^{EA}_{dyn}
4.6/100	59	40	71	11	39	40
4.6/300	87	67	110	19	60	63
76.1/100	68	39	78	14	36	38
76.1/300	102	60	118	19	54	57

[a]The samples are labeled according to the HAT-CN molar fraction and the MD simulation temperature. Low- and high-frequency fluctuations were found to be uncorrelated.

Three NPB:HAT-CN blends of increasing HAT-CN molar fraction (4.6%, 10.3%, and 76.1%) were simulated with MD simulations, adopting a non-equilibrium protocol that reproduces vapor co-deposition.[12−14,18,19] The final structure of the sample with the highest HAT-CN molar fraction at 300 K is displayed in Figure 1, showing also the two components separately to highlight the occurrence of microsegregation in the blend. The electrostatic potential maps in Figure 1 show major differences in the charge distributions of the two molecules. HAT-CN is a flat and rigid molecule, characterized by symmetrically distributed and strongly dipolar cyano groups attached to the π core. In contrast, NPB features a weakly polarized charge density and presents a dumbbell shape, together with a certain conformational freedom conferred by rotations about phenyl−phenyl and N−phenyl bonds (see Figure S1). From the differences in shape and molecular charge distribution between NPB and HAT-CN, one can surmise that their intermolecular interactions might promote phase separation with respect to the entropically favored full mixing, even in the solid state, and simulations show that this is the case. This segregation determines separate migration pathways for holes (in NPB) and electrons (in HAT-CN) from the interface to the electrodes, while still maintaining close D:A contacts (see Figure S2). However, the structural analysis of the samples ruled out the presence of any particular orientational or positional order.

Average values of the charge transport energy levels in the solid state as a function of composition and temperature are shown in Figure 2. Both IP_{NPB} and $EA_{HAT\text{-}CN}$ increase substantially and approximately linearly with the HAT-CN molar fraction, although the limited number of investigated samples does not allow us to establish whether the growth is linear like in other binary molecular blends.[20,21] As reported in Table 2, with the change from 4.6% to 76.1% HAT-CN at 300 K, the mean IP_{NPB} increases from 6.00 to 6.80 eV, with a remarkable shift of 0.8 eV due to the electrostatic interactions with HAT-CN, while the mean $EA_{HAT\text{-}CN}$ increases by 0.72 eV, from 4.24 to 4.96 eV. The increase in the IP and EA of the two

https://dx.doi.org/10.1021/acs.jpclett.0c02858
J. Phys. Chem. Lett. 2020, 11, 10219−10226

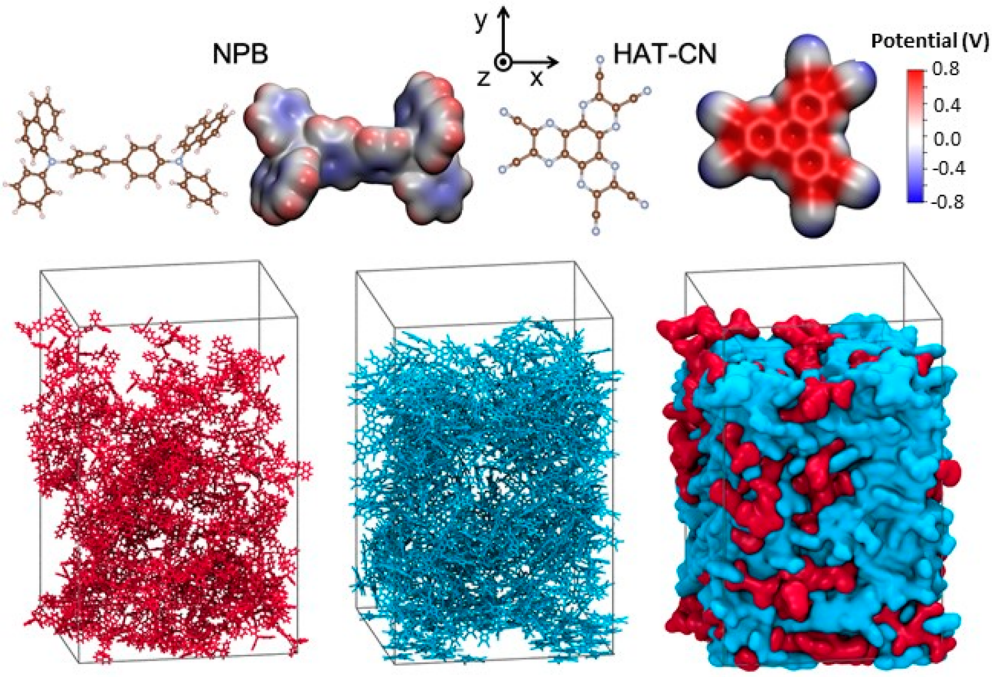

Figure 1. Molecular structures and electrostatic potential color maps of *N*,*N*′-di(1-naphthyl)-*N*,*N*′-diphenyl-(1,1′-biphenyl)-4,4′-diamine (NPB) and 1,4,5,8,9,11-hexaazatriphenylene hexacarbonitrile (HAT-CN) (top). Snapshots of the simulated sample at a 24.9:76.1 NPB:HAT-CN ratio (bottom). Visualizations of NPB molecules only (red), HAT-CN only (cyan), and the whole sample with an isosurface representation from left to right, respectively.

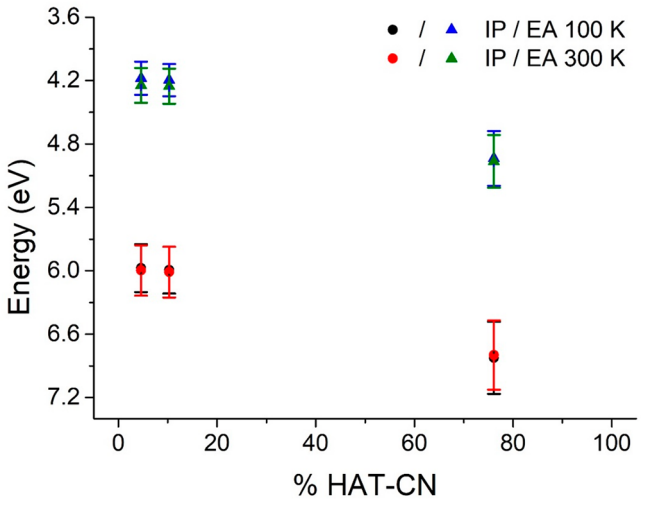

Figure 2. Average electron affinity (EA) of HAT-CN (blue and green triangles) and ionization potential (IP) of NPB (black and red circles) as a function of temperature and HAT-CN molar fraction. Vertical bars represent standard deviations. Because the shifts in the energy levels of NPB and HAT-CN are so similar, overall the photovoltaic gap $E_{GAP} = IP_{NPB} - EA_{HAT\text{-}CN}$ is not expected to change significantly with HAT-CN molar fraction (see below).

molecules in HAT-CN-rich blends is in line with similar results for the host dependence of energy levels[11] and zinc phthalocyanine blends.[20,22] In our case, the electrostatic landscape is governed by the strong quadrupole moment of the HAT-CN molecule, characterized by electron-withdrawing groups at the π core periphery, which generally leads to a stabilization of occupied and empty levels. The rather strong composition effects in Figure 2 contrast with the effect of temperature, hardly detectable considering the standard

Table 2. Average Energies of Charge Carrier Transport Levels (in electronvolts) and Standard Deviations σ^{x}_{tot} (in millielectronvolts, where x stands for IP or EA) in NPB:HAT-CN Blends at 300 K[a]

% HAT-CN	IP_{NPB}	σ^{IP}_{tot}	σ^{IP}_{conf}	σ^{IP}_{env}	σ^{IP}_{stat}	σ^{IP}_{low}
4.6	6.00	239	179	161	223	87
10.3	6.01	241	188	164	222	94
76.1	6.80	328	183	274	311	102
% HAT-CN	$EA_{HAT\text{-}CN}$	σ^{EA}_{tot}	σ^{EA}_{conf}	σ^{EA}_{env}	σ^{EA}_{stat}	σ^{EA}_{low}
4.6	4.24	165	57	151	164	19
10.3	4.25	166	47	155	165	19
76.1	4.96	249	42	244	249	19

[a]Energy fluctuations (in millielectronvolts) were also quantified according to their nature: intramolecular σ^{x}_{conf}, intermolecular σ^{x}_{env}, static σ^{x}_{stat}, and low-frequency dynamic disorder σ^{x}_{low}.

deviations of IP_{NPB} and $EA_{HAT\text{-}CN}$, suggesting a minor effect exerted by thermal fluctuations in these blends. Therefore, in the following, we will mainly focus on the results at 300 K (see Table S1 for data at 100 K).

The total energetic disorder σ^{x}_{tot} (where x stands for IP or EA) can be partitioned into different contributions, as depicted in Figure 3. Energetic disorder can be characterized in terms of its physical origin, i.e., conformational (σ^{x}_{conf}) and environmental disorder (σ^{x}_{env}), and it can also be classified according to time scales as being of static (σ^{x}_{stat}) or dynamic (σ^{x}_{low}) nature. While static disorder is mostly sourced by inhomogeneity in the electrostatic environment of the CT pairs, dynamic disorder includes contributions from intramolecular low-frequency modes (below 200 cm^{-1}) that are correctly described by our classical MD simulations in the explored temperature range. We note that, unlike recent studies addressing dynamic disorder in disordered molecular

https://dx.doi.org/10.1021/acs.jpclett.0c02858
J. Phys. Chem. Lett. 2020, 11, 10219−10226

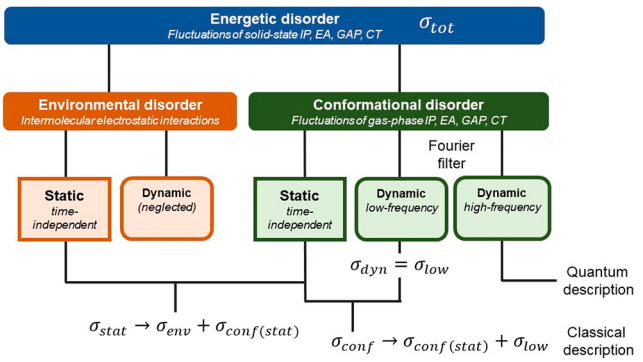

Figure 3. Logical scheme explaining the partitioning of the different contributions to the total energetic disorder σ^{x}_{tot}. DFT/ME calculations were carried out to compute IP_{NPB} and $EA_{HAT\text{-}CN}$ in the last MD frame of each blend. This yielded a distribution of charge carrier energy levels characterized by a standard deviation σ^{x}_{tot}. This contains a component related to the environmental disorder (due to intermolecular electrostatic interactions) and the other related to conformational disorder σ^{x}_{conf} (an intramolecular contribution related to different molecular geometries sampled in MD simulations), which can be extracted from gas-phase DFT fluctuations of IP and EA. In turn, σ^{x}_{conf} has two contributions: a static part and a dynamic part. The latter σ^{x}_{dyn} is composed by intramolecular low- and high-frequency components. By applying a Fourier filter to DFT time series of molecular orbital energies, computed along the MD trajectories at 300 K, we were able to distinguish between σ^{x}_{low} and σ^{x}_{high}. The latter contribution was removed from σ^{x}_{conf}, so that σ^{x}_{conf} is thus made of the static $\sigma^{x}_{conf(stat)}$ and the low-frequency dynamic σ^{x}_{low} part of the conformational disorder. With regard to the environmental one, we assumed σ^{x}_{env} to be static in time, neglecting its dynamic character. Therefore, within the static part σ^{x}_{stat}, there are both σ^{x}_{env} and $\sigma^{x}_{conf(stat)}$. The same reasoning can be extended to the case in which x stands for GAP or CT.

blends,[23−25] the IP and EA fluctuations due to high-frequency vibrations were filtered out in the calculation of energetic disorder, which accounts only for low-frequency classical modes. The contribution from high-frequency vibrations was then included in a proper quantum-mechanical framework in the calculation of the absorption spectrum and nonradiative recombination rates.

Environmental effects due to long-range intermolecular electrostatic interactions represent the predominant contribution to the total energetic disorder: σ^{x}_{env} comparably affects IP_{NPB} and $EA_{HAT\text{-}CN}$ and markedly increases with the HAT-CN molar fraction, revealing that the main source of electrostatic disorder is the strongly polarized charge density of the acceptor molecule. Instead, σ^{x}_{conf} is only weakly sensitive to composition, but different between the two molecules. The calculated σ^{x}_{conf} values are much larger for NPB, owing to the flexible molecular structure of the donor molecule as compared to the rather rigid HAT-CN acceptor. This dissimilarity between the two components is even more pronounced when looking at σ^{x}_{low}, which is the sole contribution with a clear temperature dependence, in a way compatible with that prescribed for coupled classical harmonic oscillators. In summary, electrostatic and conformational fluctuations similarly contribute to the energetic disorder in IP_{NPB}, while the spread in $EA_{HAT\text{-}CN}$ is essentially determined by the former.

The analysis of CT excitations is presented in Figure 4 and Table 3 (see Table S2 and Figure S4 for further data). Notwithstanding the large variations in the transport levels with the blend composition, mean photovoltaic gap E_{GAP} changes by <0.2 eV, going from 1.72 eV at 4.6% to 1.90 eV at 76.1% of HAT-CN. The mean energy of the first CT-state E_{CT} shows even smaller variations with composition. Exciton binding energy E_B is predicted to be approximately −0.4 eV, in line with typical values expected in organic semiconductors.[26] The large standard deviation σ^{CT}_{tot}, reaching 371 meV at 76.1% HAT-CN, is dominated by the fluctuations in the photovoltaic gap, rather than by those in the binding energy. It is largely due to the rough electrostatic landscape produced by HAT-CN molecules and to the conformational disorder of flexible NPBs, both contributions being essentially static in time. The broad distribution of CT-state energies observed experimentally in EQE spectra (see below) could be hence imputable to the energetic disorder in the hole and electron energy levels.

The existence of an important contribution from static disorder is confirmed by fits of the low-energy portion of the EQE spectra at different temperatures (see the Supporting Information for details in EQE measurements). Experimental EQE spectra are shown in Figure 5a for temperatures ranging from 110 to 296 K. A fit of EQE spectra was performed to extract the static and dynamic contributions to the total energetic disorder as a function of temperature. The linear extrapolation of $\sigma_{EQE}{}^{2}$ to 0 K (Figure 5b) provides an estimate for the static disorder of 150 meV (see Table S3), which dominates the CT spectral line width even at room temperature, quite contrary to observations on most fullerene-based OSCs, but qualitatively in agreement with the data in Table 3 for NPB:HAT-CN blends.

A quantitative comparison between the calculated and the EQE-derived disorder requires some caution. The EQE spectrum is not able to fully capture the CT DOS as shown in the striking difference with the photothermal deflection spectroscopy (PDS) spectrum: the lowest-energy transition, peaking at around 1.2 eV in the latter, is almost absent in the former (Figure 6a). To rationalize this dissimilarity, we exploit the knowledge of the CT DOS from our calculations to consider nonradiative recombination, a major source of voltage losses in OSCs.[4,30] As shown in Figure 6a (the full data set is given in Figures S5 and S6), irrespective of the blend composition, nonradiative rates κ_{NRAD} exceed 10^{12} s^{-1} for CT energies below 1.5 eV and decrease by several orders of magnitude at increasing CT energies, a trend that is reminiscent of the energy gap law.[31,32] Lowest-energy CT states strongly recombine to the ground state before charge dissociation occurs, explaining the difference in the shape of the EQE and absorption spectra. Thus, unlike higher-energy CT or Frenkel excitations, the lowest-energy CT states are photovoltaically inactive in NPB:HAT-CN blends; viz., they do not contribute to photocurrent generation and are responsible for large voltage losses.[30,32]

Therefore, EQE spectra are not fully representative of the actual CT DOS, at least in these D:A blends, as nonradiative processes crop the low-energy tails of the distributions. As such, the results of common Gaussian fits of the EQE spectral tail to extract the band maximum and width should be taken with caution. The EQE fit in Figure 6a seems to yield a peak position that is ∼0.7 eV from the first absorption peak; hence, the associated standard deviation cannot be interpreted as a measure of the energetic disorder in the lowest-energy CT state. The next question is whether optical absorption, electroluminescence (EL), or photoluminescence (PL) measurements provide a more representative proxy for the system DOS and would be more suited for quantifying the total

https://dx.doi.org/10.1021/acs.jpclett.0c02858
J. Phys. Chem. Lett. 2020, 11, 10219−10226

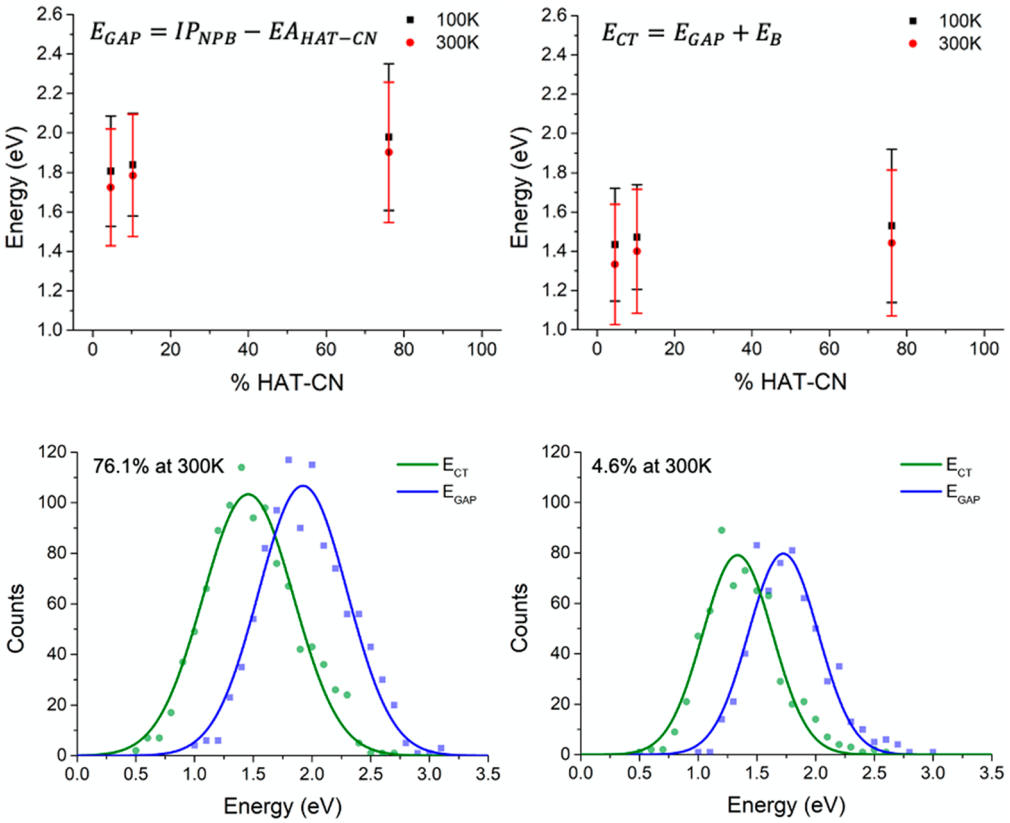

Figure 4. Average photovoltaic gap (E_{GAP}) and CT-state energies (E_{CT}) for NPB:HAT-CN pairs as a function of HAT-CN molar fraction and temperature (top). Vertical bars represent standard deviations. CT density of states (DOS) and distribution of gap energies at two different HAT-CN molar fractions at 300 K (bottom). Solid lines are Gaussian fits.

Table 3. Average Photovoltaic Gaps (E_{GAP}), CT-State (E_{CT}) and Exciton Binding Energies (E_B) (in electronvolts), and Standard Deviations (σ^x_{tot}, in millielectronvolts, where x stands for GAP or CT) for NPB:HAT-CN Pairs at 300 K as a Function of HAT-CN Molar Fraction[a]

% HAT-CN	E_{GAP}	σ^{GAP}_{tot}	σ^{GAP}_{conf}	σ^{GAP}_{env}	σ^{GAP}_{stat}	σ^{GAP}_{low}	λ_{env}
4.6	1.72	296	184	238	282	89	155
10.3	1.78	310	191	239	295	96	181
76.1	1.90	355	184	339	340	104	209
% HAT-CN	E_{CT}	σ^{CT}_{tot}	σ^{CT}_{stat}	E_B	σ_B		
4.6	1.33	306	293	−0.39	123		
10.3	1.40	316	301	−0.38	118		
76.1	1.44	371	357	−0.46	133		

[a]Energy fluctuations (in millielectronvolts) were also quantified according to their nature: intramolecular σ^x_{conf}, intermolecular σ^x_{env}, static σ^x_{stat}, and low-frequency dynamic disorder σ^x_{low}. Environmental reorganization energies λ_{env} (in millielectronvolts) were calculated as $\lambda_{env} = \frac{\sigma^{2x}_{low}}{2k_BT}$. Note that for E_{GAP} and E_{GAP} the intermolecular σ^x_{env} and low-frequency dynamic disorder σ^x_{low} coincide and thus are given just once.

energetic disorder. Figure 6b compares the experimental and calculated absorption spectra and the CT DOS. The calculated absorption matches well with experiment, capturing the peak position, yet overestimating the bandwidth, and giving a close reproduction of the CT DOS low-energy tail. These results suggest that absorption spectra, although more challenging to collect experimentally for weakly absorbing intermolecular excitons, can provide a faithful description of the CT DOS in D:A blends, in a manner independent of the spectral region. In contrast, emission spectra suffer from the competition with nonradiative processes as does EQE and should thus be interpreted equally with care.

The origin for the CT energetic disorder in OSCs was recently debated in the literature.[4−6] Different conclusions regarding the relative contributions from static versus dynamic disorder were reached in papers on D:A blends based on fullerene derivatives. Comparable static and dynamic disorder was found for polymer:phenyl-C61-butyric acid methyl ester ($PC_{61}BM$) blends,[33] while a picture solely based on dynamic disorder due to low-frequency intramolecular mode was able to correctly describe small molecule-C_{60} systems.[27] For the latter, the evidence for a temperature-independent energetic disorder was very recently ascribed to the zero-point motion of quantum vibrational modes.[6] Besides raising some concerns about the experimental determination of the disorder, our microscopic analysis suggests that the answer to the paramount question regarding the nature of the disorder depends markedly on the investigated system and on the way it is probed. If it is plausible that the static environmental disorder is almost negligible for blends of donor molecules diluted in electrically neutral fullerenes, this contribution can be substantial in the presence of molecules featuring polar groups, such as the NPB:HAT-CN system, and whose broad CT-state spectral signature is mostly due to static disorder.

The nature of low-lying CT states in NPB:HAT-CN D:A blends was investigated with a multiscale computational approach. We found that the wide CT DOS broadening is dominated by static disorder and arises from both conforma-

https://dx.doi.org/10.1021/acs.jpclett.0c02858
J. Phys. Chem. Lett. 2020, 11, 10219−10226

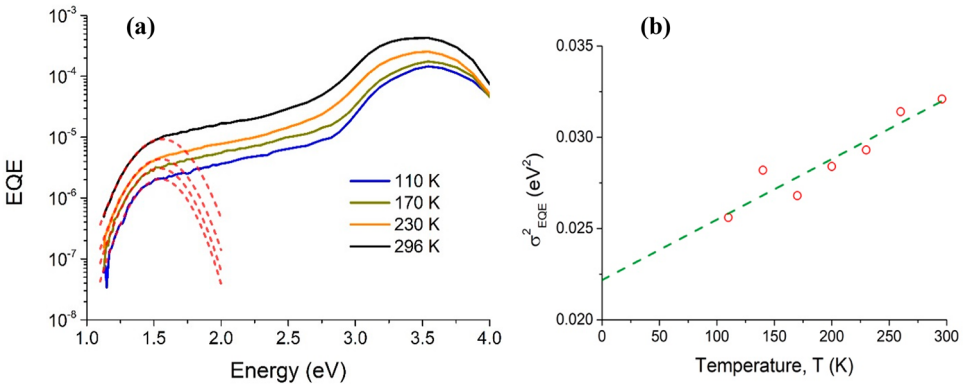

Figure 5. (a) Temperature-dependent external quantum efficiency (EQE) spectra of a NPB:HAT-CN BHJ OSC with 66.0% HAT-CN (solid lines). With a decrease in temperature, the EQE steadily decreases as the generation and transport of charge carriers become increasingly difficult.[27,28] Despite the decrease in magnitude, the EQE spectral shape is mostly preserved but has a small red-shift of the lowest-energy CT peak with a decrease in temperature. Lowest-energy CT spectra were fitted, following the approach of Burke et al.,[29] considering a Gaussian CT energetic distribution (dashed red lines). (b) Temperature dependence of the variance of the energetic disorder extracted from a Gaussian fit of EQE spectra. The extrapolation to 0 K (dashed green line) allows us to estimate a static, temperature-independent, disorder of 150 meV.

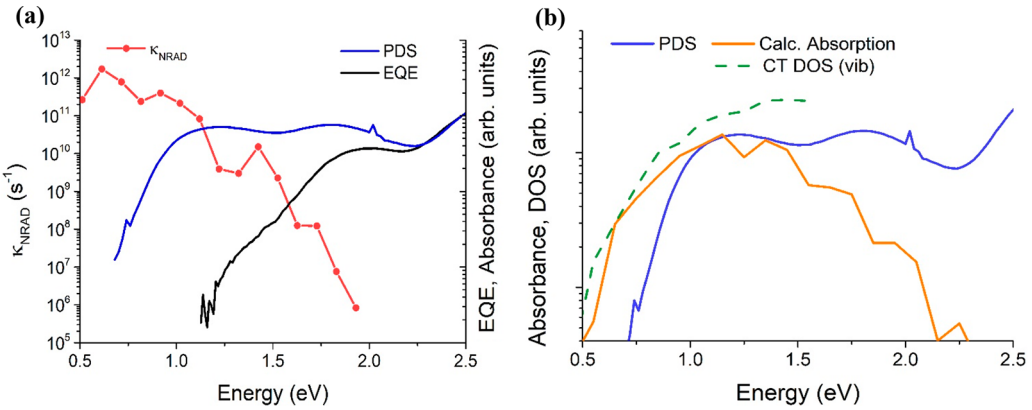

Figure 6. (a) EQE spectrum (solid black line) and absorptance spectrum (solid blue line) of a NPB:HAT-CN film measured by photothermal deflection spectroscopy (PDS).[8] Red points show the average calculated nonradiative decay rates of CT excitations to the ground state, binned over small (100 meV) energy intervals. The 6 order of magnitude drop of κ_{NRAD} in the CT-state energy window rationalizes the stark difference between EQE and PDS spectra. (b) PDS spectrum compared to the calculated one (solid orange line) and to the calculated vibrationally broadened CT density of states (DOS) (dashed green line). Experimental and calculated data refer to samples with 4.6% HAT-CN at 300 K.

tional and electrostatic landscape variations, which originate from NPB flexibility and HAT-CN quadrupoles. The large broadening and the deep HAT-CN LUMO levels ensure that a large portion of the CT DOS lies below 1.5 eV, where nonradiative decay to the ground state becomes predominant over charge separation. This energetic situation has two important consequences. (i) The tail of the CT DOS cannot be probed via EQE, EL, or PL measurements, and more importantly for OSCs, it does not contribute to charge generation but rather to recombination; (ii) in such a case, the standard procedure of fitting the EQE signal tail with a Gaussian function to extract static and dynamic disorder becomes unreliable.

■ ASSOCIATED CONTENT

Supporting Information

The Supporting Information is available free of charge at https://pubs.acs.org/doi/10.1021/acs.jpclett.0c02858.

Molecular dynamics simulation; electronic structure calculations; EQE measurements; distribution of NPB dihedrals at different temperatures; mixed NPB:HAT-CN radial distribution functions; time fluctuations and Fourier transform of orbital energies; average IP, EA, gap, and CT energies and standard deviations at 100 K; CT DOS at 100 and 300 K; electronic couplings and nonradiative rates at 300 K; fitting of effective lowest CT-state and reorganization energies; and static (σ_{stat}) and dynamic (σ_{dyn}) disorder contribution to the CT EQE spectral broadening (PDF)

■ AUTHOR INFORMATION

Corresponding Author

David Beljonne − *Laboratory for Chemistry of Novel Materials, University of Mons, 7000 Mons, Belgium;* orcid.org/0000-0002-2989-3557; Email: David.Beljonne@umons.ac.be

Authors

Giacomo Londi − *Laboratory for Chemistry of Novel Materials, University of Mons, 7000 Mons, Belgium*

Saeed-Uz-Zaman Khan − *Department of Electrical Engineering, Princeton University, Princeton, New Jersey 08544, United States*

https://dx.doi.org/10.1021/acs.jpclett.0c02858
J. Phys. Chem. Lett. 2020, 11, 10219−10226

Luca Muccioli − *Department of Industrial Chemistry, University of Bologna, 40136 Bologna, Italy;* orcid.org/0000-0001-9227-1059

Gabriele D'Avino − *Grenoble Alpes University, CNRS, Grenoble INP, Institut Néel, 38042 Grenoble, France;* orcid.org/0000-0002-5897-2924

Barry P. Rand − *Department of Electrical Engineering and Andlinger Center for Energy and the Environment, Princeton University, Princeton, New Jersey 08544, United States;* orcid.org/0000-0003-4409-8751

Complete contact information is available at: https://pubs.acs.org/10.1021/acs.jpclett.0c02858

Notes

The authors declare no competing financial interest.

■ ACKNOWLEDGMENTS

This study received funding from the European Union's Horizon 2020 research and innovation program under Marie Skłodowska-Curie Grant Agreement 722651 (SEPOMO project) and from the European Union's Horizon 2020 research and innovation programme under Grant Agreement 646176 (EXTMOS). L.M. thanks MIUR for financial support through PRIN Project 2015XJA9NT "Molecular Organization in Organic Thin Films via Computer Simulation of their Fabrication Processes". Computational resources were provided by the Consortium des Équipements de Calcul Intensif (CÉCI), funded by the Fonds de la Recherche Scientifique de Belgique (F.R.S.-FNRS) under Grant 2.5020.11, as well as the Tier-1 supercomputer of the Fédération Wallonie-Bruxelles, infrastructure funded by the Walloon Region under Grant Agreement 1117545. G.L., L.M., G.D., and D.B. gratefully thank Xavier Blase for fruitful discussions on many-body perturbation theory and for sharing the FIESTA code. D.B. is a FNRS Research Director. S.-U.-Z.K. and B.P.R. acknowledge the U.S. Department of Energy, Office of Basic Energy Sciences, for Award DE-SC0012458.

■ REFERENCES

(1) Liu, Q.; et al. 18% Efficiency Organic Solar Cells. *Sci. Bull.* **2020**, *65* (4), 272−275.

(2) Cui, Y.; et al. Single-Junction Organic Photovoltaic Cells with Approaching 18% Efficiency. *Adv. Mater.* **2020**, *32*, 1908205.

(3) Fusella, M. A.; et al. Band-like Charge Photogeneration at a Crystalline Organic Donor/Acceptor Interface. *Adv. Energy Mater.* **2018**, *8* (9), 1701494.

(4) Lin, Y. L.; Fusella, M. A.; Rand, B. P. The Impact of Local Morphology on Organic Donor/Acceptor Charge Transfer States. *Adv. Energy Mater.* **2018**, *8* (28), 1702816.

(5) Vandewal, K.; et al. Efficient Charge Generation by Relaxed Charge-Transfer States at Organic Interfaces. *Nat. Mater.* **2014**, *13* (1), 63−68.

(6) Panhans, M.; Hutsch, S.; Benduhn, J.; Schellhammer, K. S.; Nikolis, V. C.; Vangerven, T.; Vandewal, K.; Ortmann, F. Molecular Vibrations Reduce the Maximum Achievable Photovoltage in Organic Solar Cells. *Nat. Commun.* **2020**, *11* (1), 1488.

(7) Lin, Y. L.; Fusella, M. A.; Kozlov, O. V.; Lin, X.; Kahn, A.; Pshenichnikov, M. S.; Rand, B. P. Morphological Tuning of the Energetics in Singlet Fission Organic Solar Cells. *Adv. Funct. Mater.* **2016**, *26* (35), 6489−6494.

(8) Khan, S. U. Z.; et al. Multiple Charge Transfer States in Donor-Acceptor Heterojunctions with Large Frontier Orbital Energy Offsets. *Chem. Mater.* **2019**, *31* (17), 6808−6817.

(9) D'Avino, G.; Muccioli, L.; Zannoni, C.; Beljonne, D.; Soos, Z. G. Electronic Polarization in Organic Crystals: A Comparative Study of Induced Dipoles and Intramolecular Charge Redistribution Schemes. *J. Chem. Theory Comput.* **2014**, *10* (11), 4959−4971.

(10) D'Avino, G.; Muccioli, L.; Castet, F.; Poelking, C.; Andrienko, D.; Soos, Z. G.; Cornil, J.; Beljonne, D. Electrostatic Phenomena in Organic Semiconductors: Fundamentals and Implications for Photovoltaics. *J. Phys.: Condens. Matter* **2016**, *28* (43), 433002.

(11) Li, J.; et al. Host Dependence of the Electron Affinity of Molecular Dopants. *Mater. Horiz.* **2019**, *6* (1), 107−114.

(12) Muccioli, L.; D'Avino, G.; Zannoni, C. Simulation of Vapor-Phase Deposition and Growth of a Pentacene Thin Film on C60 (001). *Adv. Mater.* **2011**, *23* (39), 4532−4536.

(13) D'Avino, G.; Muccioli, L.; Zannoni, C. From Chiral Islands to Smectic Layers: A Computational Journey Across Sexithiophene Morphologies on C 60. *Adv. Funct. Mater.* **2015**, *25* (13), 1985−1995.

(14) Roscioni, O. M.; D'Avino, G.; Muccioli, L.; Zannoni, C. Pentacene Crystal Growth on Silica and Layer-Dependent Step-Edge Barrier from Atomistic Simulations. *J. Phys. Chem. Lett.* **2018**, *9* (23), 6900−6906.

(15) Phillips, J. C.; Braun, R.; Wang, W.; Gumbart, J.; Tajkhorshid, E.; Villa, E.; Chipot, C.; Skeel, R. D.; Kalé, L.; Schulten, K. Scalable Molecular Dynamics with NAMD. *J. Comput. Chem.* **2005**, *26* (16), 1781−1802.

(16) Lin, Y. S.; Li, G. De; Mao, S. P.; Chai, J. Da. Long-Range Corrected Hybrid Density Functionals with Improved Dispersion Corrections. *J. Chem. Theory Comput.* **2013**, *9* (1), 263−272.

(17) Frisch, M. J.; et al. *Gaussian 16*, rev. C.01; Gaussian Inc.: Wallingford, CT, 2016.

(18) Tonnelé, C.; et al. Elucidating the Spatial Arrangement of Emitter Molecules in Organic Light-Emitting Diode Films. *Angew. Chem., Int. Ed.* **2017**, *56* (29), 8402−8406.

(19) Lee, T.; Sanzogni, A.; Zhangzhou, N.; Burn, P. L.; Mark, A. E. Morphology of a Bulk Heterojunction Photovoltaic Cell with Low Donor Concentration. *ACS Appl. Mater. Interfaces* **2018**, *10* (38), 32413−32419.

(20) Schwarze, M.; et al. Band Structure Engineering in Organic Semiconductors. *Science (Washington, DC, U. S.)* **2016**, *352* (6292), 1446−1449.

(21) Graham, K. R.; et al. The Roles of Structural Order and Intermolecular Interactions in Determining Ionization Energies and Charge-Transfer State Energies in Organic Semiconductors. *Adv. Energy Mater.* **2016**, *6* (22), 1601211.

(22) Privitera, A.; Londi, G.; Riede, M.; D'Avino, G.; Beljonne, D. Molecular Quadrupole Moments Promote Ground-State Charge Generation in Doped Organic Semiconductors. *Adv. Funct. Mater.* **2020**, *30*, 2004600.

(23) Tummala, N. R.; Zheng, Z.; Aziz, S. G.; Coropceanu, V.; Brédas, J.-L. Static and Dynamic Energetic Disorders in the C60, PC61BM, C70, and PC71BM Fullerenes. *J. Phys. Chem. Lett.* **2015**, *6* (18), 3657−3662.

(24) D'Avino, G.; Olivier, Y.; Muccioli, L.; Beljonne, D. Do Charges Delocalize over Multiple Molecules in Fullerene Derivatives? *J. Mater. Chem. C* **2016**, *4* (17), 3747−3756.

(25) de Silva, P.; Van Voorhis, T. QM/MM Study of Static and Dynamic Energetic Disorder in the Emission Layer of an Organic Light-Emitting Diode. *J. Phys. Chem. Lett.* **2018**, *9* (6), 1329−1334.

(26) Mikhnenko, O. V.; Blom, P. W. M.; Nguyen, T. Q. Exciton Diffusion in Organic Semiconductors. *Energy Environ. Sci.* **2015**, *8*, 1867−1888.

(27) Tvingstedt, K.; Benduhn, J.; Vandewal, K. Temperature Dependence of the Spectral Line-Width of Charge-Transfer State Emission in Organic Solar Cells; Static vs. Dynamic Disorder. *Mater. Horiz.* **2020**, *7* (7), 1888.

(28) Baranovskii, S. D. Theoretical Description of Charge Transport in Disordered Organic Semiconductors. *Phys. Status Solidi B* **2014**, *251* (3), 487−525.

(29) Burke, T. M.; Sweetnam, S.; Vandewal, K.; McGehee, M. D. Beyond Langevin Recombination: How Equilibrium Between Free Carriers and Charge Transfer States Determines the Open-Circuit

Voltage of Organic Solar Cells. *Adv. Energy Mater.* **2015**, *5* (11), 1500123.
(30) Azzouzi, M.; Yan, J.; Kirchartz, T.; Liu, K.; Wang, J.; Wu, H.; Nelson, J. Nonradiative Energy Losses in Bulk-Heterojunction Organic Photovoltaics. *Phys. Rev. X* **2018**, *8* (3), 031055.
(31) Bixon, M.; Jortner, J.; Cortes, J.; Heitele, H.; Michel-Beyerle, M. E. Energy Gap Law for Nonradiative and Radiative Charge Transfer in Isolated and in Solvated Supermolecules. *J. Phys. Chem.* **1994**, *98* (30), 7289−7299.
(32) Benduhn, J.; et al. Intrinsic Non-Radiative Voltage Losses in Fullerene-Based Organic Solar Cells. *Nat. Energy* **2017**, *2* (6), 17053.
(33) Kahle, F. J.; Rudnick, A.; Bässler, H.; Köhler, A. How to Interpret Absorption and Fluorescence Spectra of Charge Transfer States in an Organic Solar Cell. *Mater. Horiz.* **2018**, *5* (5), 837−848.

https://dx.doi.org/10.1021/acs.jpclett.0c02858
J. Phys. Chem. Lett. 2020, 11, 10219−10226